Micro- and nanostructural details of the spider's mechanical vibration filter. Relevance for low frequency signal transmission.

Maxim Erko[1], Osnat Younus-Metzler[1], Alexander Rack[2], Paul Zaslansky[3], Seth L. Young[4], Garrett Milliron[1] Marius Chyasnavichyus[4], Friedrich G. Barth[5], Peter Fratzl[1], Vladimir Tsukruk[4], Igor Zlotnikov[1], Yael Politi[1,*]

**Corresponding Author Email: yael.politi@mpikg.mpg.de*

[1]*Department of Biomaterials, Max Planck Institute of Colloids and Interfaces, Research Campus Golm, 14424 Potsdam, Germany.*

[2]*European Synchrotron Radiation Facility, 38043 Grenoble, France*

[3]*Charite, Berlin Brandenburg Ctr Regenerat Therapies, Julius Wolff Inst, D-13353 Berlin, Germany*

[4]*School of Materials Science and Engineering, Georgia Institute of Technology, Atlanta, Georgia 30332, United States of America*

[5]*Department of Neurobiology, Faculty of Life Sciences, University of Vienna, 1090 Vienna, Austria.*

1. Introduction

Mechano-sensing is ubiquitous in Nature. Examples are hearing, tactile and vibration sensing, the sensing of air and water flow, strain and stretch. Mechano-sensing in Arachnids, in general and in spiders in particular, is well recognized for its high sensitivity and specificity (Barth 2002; Barth 2004; Fratzl and Barth 2009). The spiders' strain detectors, the so-called slit-sensilla, are elongated openings within the exoskeleton, innervated by sensory cells and often located in the vicinity of joints in the leg or elsewhere (Barth 1972; Barth 1972; Barth 2012; Barth 2012). They are widespread among spiders and share some similarity to the campaniform strain sensors of insects. The metatarsal lyriform organ of the Central American wandering spider *Cupiennius salei* forms a close and roughly parallel array of 21 slits. It is the spider's main vibration detector (Barth and Geethabali 1982; Speck and Barth 1982; Speck-Hergenroder and Barth 1988). It is responsible for sensing vibration signals originating from predators, prey, or courting partners with extraordinary sensitivity (Hergenroder and Barth 1983; Gingl, Burger et al. 2006). These vibration stimuli are usually of comparatively high frequency (40 - several hundred Hz). In addition the metatarsal lyriform organ responds to low frequency vibrations (0.1 - 40 Hz) with nervous impulses, although with much lower sensitivity (Barth and Geethabali 1982). Such low frequency stimuli occur during locomotion and other activities (Barth and Bohnenberger 1978). Taken together, the range of frequencies detected by the slits spans as much as three orders of magnitude.

The metatarsal lyriform organ is situated at the distal end of the second last segment of each leg, i.e. their metatarsus (Figure 1). Substrate vibrations deflect the most distal leg segment, the tarsus, which transmits the signal to the vibration sensitive slit sensilla by pressing against the metatarsus. A cuticular pad (Figure 1B-D) is situated just in front of the metatarsal lyriform organ, at the contact area with the tarsus. The pad plays a major role in the mechanical filtering of vibrational stimuli and represents an effective high-pass filter (McConney, Schaber et al. 2009). This latter function was recently mapped to the external most layer of the pad, a layer of epicuticle (Young, Chyasnavichyus et al. 2014). This layer is unusually thick and behaves visco-elastically. Its glass transition temperature is around 19°C, corresponding to a frequency of 100 Hz according to the time-temperature-modulus relationship in viscoelastic materials.

In its natural habitat and during its time of activity the spider sits on a leaf in its characteristic “hunting position”, with the proximal end of the tarsus just in contact with the pad. From this point of contact onwards, further deflection of the tarsus will elicit action potentials in the sensory cells of the metatarsal lyriform organ - if its amplitude is above threshold (depending on frequency) and overcomes the filtering restrictions of the pad. Electrophysiological studies have shown that for high frequencies only minute deflections of the tarsus beyond the “first contact” with the pad are needed in order to elicit action potentials. In particular, for frequencies of several hundred Hz vertical threshold displacements of the substrate down to the order of nanometers and corresponding to deflection angles of around 0.01° from the “first contact” angle elicit physiological responses in the receptor cell (Molina, Schaber et al. 2009). Below stimulus frequencies of about 40Hz, however, threshold deflections of the tarsus by tens of microns or up to 10° from the “first contact” position are needed in order to elicit a nervous response.

The remarkably high sensitivity of the slits at high frequencies is owed first to the properties of the epicuticular layer of the pad, which assumes a glassy state at these frequencies, thus efficiently transmitting the signal (Young, Chyasnavichyus et al. 2014). Other mechanical factors affecting the mechanical sensitivity of the slits at a subsequent stage of stimulus transmission are slit length, aspect ratio and specific location within the array of slits as previously documented in detail (Hossl, Bohm et al. 2007; Schaber, Gorb et al. 2011; Barth 2012). The question remains, how low frequency stimuli are transmitted to the slits considering that the epicuticle then assumes a rubbery state, strongly damping the incoming vibrations. In addition, since large deflection amplitudes are involved, what protects the delicate slit system from damage?

Here we address these questions by studying the structure and composition of the pad and relating them to the material's mechanical properties. We also monitor the three-dimensional deformation behavior of the pad upon the static application of mechanical load similar to the natural load application at low frequencies. Thus the tarsus was deflected against the pad during X-ray micro-computer tomography (µCT) measurements in wet state. We show that the three-dimensional morphology and specifically sub-structure of the pad allows large tarsal deflections to be converted into small displacements at the pad-slit contact region, thus allowing transmission of low frequencies stimuli while providing mechanical robustness and damage protection at high loads.

Materials and methods

Sample preparation

Adult females of the Central American wandering spider *Cupiennius salei* (Barth 2002) were received from the breeding stock of the Department of Neurobiology of the University of Vienna. In all experiments, except in those applying micro-computer tomography (µCT), we used spider legs taken from shock frozen (at -196°C) specimens initially anaesthetized and kept at around -18° C until use. For µCT experiments fresh autotomized spider legs were prepared. For a better view the hairs covering the metatarsus were removed by gently wiping the surface with a cotton tissue. All experiments we performed according to the German animal welfare act §8a(4).

Sectioning: For X-ray scattering experiments and Confocal Laser Scanning Microscopy (CLSM) the pad was dissected from the tarsus and sectioned into 30 µm thick slices using a vibratome (Leica VT1000S; Leica Microsystems GmbH, Wetzlar, Germany) at 80 Hz steel blade frequency and 0.025 mm/s blade velocity. For sectioning, the metatarsus was glued to a plastic substrate using a tiny superglue droplet (Roti coll 1, Carl Roth, Karlsruhe, Germany). Contamination of the pad region with the superglue was avoided by fixing the metatarsus sufficiently away from its dorsal side where the pad and the slits are situated. The slices were cut in high-purity water at 20° C and kept wet until the time of the experiment. The entire sample preparation process took only few minutes and was performed shortly before each measurement.

Embedding and polishing: For Scanning Acoustic Microscopy (SAM) measurements and for Nanoindentation the metatarsus containing the pad was immersed in methylmetacrylate (MMA) for 8 h followed by polymerization in an oven at 60 °C. The embedded samples were gently polished (in their sagittal plane) until the cuticular pad region

of interest was exposed to the surface. Although incubation in MMA and heating to 60°C cause drying of the samples, after sectioning and polishing the samples were rehydrated (considerable swelling was observed) in order to measure the properties of the sample as close as possible to their natural state. We expect limited influence of the embedding material (reduced mechanical modulus of 4 GPa) on the measured mechanical properties of the cuticle since, we do not observe significant infiltration of MMA into the sample as judged from the fact that the sample can be easily detached from the embedding material and that the swelling behavior is not affected.

Optical microscope imaging

Optical images were taken using a light microscope equipped with a digital camera (Dage-MTI XLM high-resolution, cooled) at 10x magnification under dark field illumination. The clarity of each optical image was digitally enhanced by focus stacking using Helicon Focus version 5.3.14 software. Hereby, more than 100 images recorded at different focal planes were superimposed giving a single high-resolution image.

Polarized light images (1388 x 1038 pixel; 0.37 µm/pixel) were recorded on an upright microscope (Axio Imager A2, Zeiss, Jena, Germany) equipped with a 20x objective (LD A-Plan 20x/0.35 Ph2) (Zeiss, Jena, Germany) using a polarizer and an analyzer with a relative orientation of 90°. The images were analyzed using the software package Zen 2012 (Zeiss, Jena, Germany).

Electron Microscopy

Scanning electron microscopy (SEM) images were taken in high vacuum ($7.5\ 10^{-8}$ Torr) using a field emission scanning electron microscope JEOL JSM-7500F in low-magnification mode. The pad samples were mounted on an SEM sample-holder with conductive carbon tape. The measurements were performed at working distance of 11.6 mm and at 5.0 kV.

Confocal laser scanning microscopy (CLSM)

Free standing pad sections (30 µm thick) were imaged on a Leica TCS SP5 (Leica Microsystems GmbH, Wetzlar, Germany) equipped with an inverted microscope (Leica DM IRBE) and two visible light lasers (wavelengths 488 nm, Argon, 100 mW; 561 nm, diode pumped solid state DPSS, 10 mW). For each sample the most appropriate lens was chosen depending on sample size. The excitation wavelengths and the wavelengths of the emitted

fluorescence were chosen according to previous studies of arthropod cuticle (Michels 2007). The power of each laser was reduced to 2 mW to avoid damage of the sample. The signal detection gain was optimized for each sample individually. The lenses and settings used for the visualization of each sample are given within the respective figure caption. Image data processing was performed using ImageJ software (Rasband 1997-2013). The auto-fluorescence images represent superimposed emission signals resulting from 488 nm and 561 nm excitation wavelengths assigned to the green and the red software channel, respectively.

Micro-computer tomography (µCT)

The experiments were performed at the European Synchrotron Radiation Facility (ESRF) in Grenoble, France, utilizing the imaging setup at beamline ID19. In order to find a compromise between high imaging sensitivity and low radiation damage the samples were measured at 25 keV photon energy (Weitkamp, Tafforeau et al. 2010). A so-called single-harmonic undulator (u13, gap 11 mm) with a narrow bandwidth was used as radiation source with a diamond filter and a Be window as the only mandatory optical elements in the beam path, leading to a homogeneous wave front at the position of the experiment and therefore excellently suited for X-ray phase contrast imaging in parallel-beam geometry. Approximately 35 mm downstream of the specimen a high-resolution indirect imaging detector was placed. It was equipped with a 8.8 µm thin single-crystal scintillator (Tb-doped Lu2SiO5), a 10x objective (0.3 numerical aperture), a 2x eye-piece and the ESRF custom made CCD camera FReLoN (type: A7899), operating with a nominal effective pixel size of 0.7 µm (Douissard, Cecilia et al. 2010). The exposure time was set to 0.2 s for each of 1000 projection images while rotating the sample over 180°. Pad morphology data were reconstructed using the ESRF software package PyHST_2 (Mirone, Brun et al. 2014), which includes a phase-retrieval using Paganin's approach (Weitkamp, Haas et al. 2011). For data visualization and segmentation ZIBAmira software (Zuse Institute, Berlin, Germany; FEI Visualization Science Group, Burlington MA, USA) was used.

The most distal two leg segments of freshly autotomized spider legs were separated from the rest of the leg using a scalpel. In order to avoid drying, the fresh cut was instantly sealed with a droplet of candle wax. The samples, now containing only metatarsus and tarsus, were mounted in a micro tomography fatigue press (Tomo-press) developed at ESRF (Bleuet, Roux et al. 2004). The metatarsus was fixed horizontally on one side of the Tomo-press while the free-hanging tarsus was pointing towards the opposite side, where a rectangular aluminum wedge was mounted. Using a remote control the wedge was brought closer towards the tarsus

thus pushing it against the pad as in natural stimulation. The desired deflection angle between the tarsus and the metatarsus (between 0° and 45°) was adjusted by horizontally changing the distance between the two fixed parts. The corresponding vertical displacement of the tarsus distal side (substrate displacement) was calculated by measuring the angle between the two leg-segments from digital images of the camera connected via a C-mount to a microscope with long working distance. A series of rotation angles was used to avoid perspective errors. The maximum angle value of 45° was defined by the geometry of the aluminum wedge. The angular deflection values were chosen according to previously reported values well within the physiological working range of the slits (Molina, Schaber et al. 2009). The tarsus was thus deflected against the metatarsus in a stepwise manner, and µCT data sets were obtained at each stationary position after one hour relaxation time for each step. For tomography measurements the sample was rotated around the horizontal axis while keeping the distance between the leg sample and the wedge constant. The Tomo-press chamber was sealed with Kapton foil and was kept humid by a continuous stream of fully hydrated air during the entire course of the measurements. Two tarsus-metatarsus joints were measured, at six and at three angular positions, respectively. The temperature inside the hutch was maintained at 20°C, which is above the glass transition temperature of the epicuticle (Young, Chyasnavichyus et al. 2014).

X-ray scattering

X-ray scattering experiments were performed at the µ-spot beamline at the BESSY II synchrotron radiation facility in Berlin, Germany. The wavelength of 0.826 Å (energy 15 keV) was selected using a multilayer monochromator. The beam was focused by a toroidal mirror and the scattering patterns were collected on the area detector (MarCCD 225, MarUSA, Evanston) with 3072 x 3072 pixels placed behind the sample. The sample-detector distance was 0.408 m and the beam diameter at the sample position was 10 µm. This gives a covered range of scattering vectors of 0.4 $nm^{-1} < q < 25\ nm^{-1}$, defined by $q = 4\pi \sin(\theta) / \lambda$, where 2θ is the scattering angle and λ the wavelength of the incident beam. All measurements were calibrated using a quartz powder placed at the sample position. For the analysis of the two-dimensional scattering data the software Fit2D (Hammersley, Svensson et al. 1994) was used.

Scanning acoustic microscopy (SAM)

SAM measurements were performed using KSISAM2000 by Krämer Scientific Instruments (Herborn, Germany) and data was collected using software MATSAM custom made by the Q-BAM Laboratory (University of Halle-Wittenberg, Germany). Temperature in the room was maintained at 21° C. Two spider leg samples had been previously embedded in MMA. After polishing (removing one half of the metatarsus) the sample surface represented the sagittal plane of the pad. The SAM analysis of this surface was performed under deionized water using 400 Hz and 820 Hz, respectively.

Nanoindentation

Nanoindentation measurements were performed using Ubi1 Nano Indenter (Hysitron, Minneapolis, MN, USA). The same samples were used as for SAM. After choosing regions for measurements using a built-in light microscope, the samples were immersed in water and allowed to equilibrate for 30 min. In this time the samples swelled considerably. The measurements were performed under water with the Berkovich tip immersed in deionized water. The following load function was applied: loading/unloading rates: 100 µN s^{-1}, holding time 60 s at a peak load of 500 µN. Each measurement included 64 indents at the respective pad region. The values for the reduced elastic modulus E_r and for hardness H were obtained from the load–displacement curves according to the Oliver and Pharr method (Oliver and Pharr 1992). They represent mean values ± standard deviation of 60 indents per region.

2. Results and Discussion

Pad morphology and deformation during load

The three-dimensional shape of the pad is rather complex (Figure 2): It has a crescent-like shape and a lumen filled with cellular materials showing slightly lighter contrast in the µCT data. Just below the lyriform organ a small cuticular "ridge" extends along a plane perpendicular to the leg long axis, which is roughly parallel to that of the slits. We refer to this ridge as "appendix". Figure 2A shows the pad surface according to µCT data (green) with three sub-regions marked in different colors. These regions specify the location and orientation of 3 types of sections used in our compositional and structural analyses. The outlines of each section are also depicted schematically in Figure 2B. In Figure 2C-H six sagittal virtual sections of the reconstructed three-dimensional pad structure (extending laterally from the center of the pad) illustrate its structure.

In order to better visualize and quantify the deformation of the pad under loads relevant to the transmission of low frequency stimuli to the slits we performed X-ray micro-tomography measurements (under hydrated conditions) of the pad in compressed state, stimulated by deflecting the tarsus against the pad. The angle formed by the long axes of tarsus and metatarsus at which the tarsus first touches the pad is defined as the "mechanical threshold angle" (see (Barth and Geethabali 1982) and (Molina, Schaber et al. 2009) measures 28° (± 1°). From now on we refer to this angle as 0° when deflecting the tarsus against the metatarsus. We measured six different angular positions between -4° and 9° (±1°). The corresponding µCT virtual slices along the long axis of the leg are given in SI Figure 2. For angles above 0° the tarsus pushes into the pad, significantly deforming its distal part. We quantified this deformation my measuring the distance of the distal surface of the pad at each degree from its resting position at 0° (Table 1). Thus, for example, at 9° ± 1°, the pad surface is pushed in 29.4 ± 0.7 µm. Figure 3D-E show that other parts of the pad hardly change their shape. However, small displacements of a few micrometers (3.5 ± 0.7 µm at 9° ± 1°) at the contact region with the slits can be seen. In addition, the slits themselves are also compressed up to 50-60% of their initial width (width of the most distal slit at 9° ± 1° in Figure 3 D-E) in agreement with a previous white light interferometry study (Schaber, Gorb et al. 2011). Importantly, the slits are compressed evenly throughout their length and depth. Another interesting observation from Figure 3B is that the contact area of the tarsus and the pad, is limited to a rather small region. When the pad is loaded by a lateral deflection, the lateral regions of the pad assume the maximum deformation (Figure 3C and SI Figure 2). Such

deflections do occur during natural stimulations and are also known to elicit action potentials (Barth 2002).

Pad sclerotization pattern

Figure 1C shows the dorsal view of an intact pad. The different colors of the distal and dorsal sides of the pad suggest different degrees of sclerotization, the darker color often being associated with higher sclerotization (Andersen 2010). While the surface is bright creamy-colored distally (blue arrow in Figure 1C), it is darker dorsally (red arrow). Auto-fluorescence measurements performed with a confocal laser-scanning microscope (CLSM) and two different excitation wavelengths support the assumption regarding the different degrees of sclerotization. In Figure 1D the emission signal images collected at 499-555 nm (green channel) and 578-678 nm (red channel) for excitation at 488 and 561 nm, respectively, are overlaid to form one composite image. Whereas the distal surface of the pad shows a predominantly green channel auto-fluorescence signal, usually attributed to cuticles with low sclerotization levels, the dorsal surface shows a strong auto-fluorescence signal in the red channel, indicative of cuticle sclerotization (Michels and Gorb 2012).

CLSM was also applied to a pad section cut along the sagittal plane. The section was first measured hydrated and again after allowing it to dry for 30 min at room temperature (Figure 4). The auto-fluorescence pattern of the pad section is rather complex compared to what is commonly found in the spider's exoskeleton, e.g. along the metatarsus (Figure 4C). While the distal part of the pad is dominated by green-channel fluorescence and contains an internal inner region with only weak fluorescence the dorsal part and the "appendix" are predominantly showing auto-fluorescence in the red channel. Interestingly, a pronounced dark-red region in the inner part of the distal pad region is observed. Such strongly sclerotized internal cuticle is not common in arthropods, except in structures like muscle attachment sites or clerites (Barth 2002). The level of sclerotization in the metatarsus away from the pad region decreases from exocuticle inwards to meso- and endocuticle following a well-known pattern common in arthropods (Barth 1969; Andersen 2010) (Figure 4C). After dehydration, CLSM images show large shrinkage in less sclerotized cuticle regions (Figure 4B) while highly sclerotized cuticle regions retain similar shape regardless of the water content. The largest effect is seen in the distal part of the pad, which shrinks to about half of its original size.

Chitin and protein distribution and alignment

X-ray scattering measurements were performed with 30 µm thick pad slices in hydrated and dry states, using a focused beam measuring 10 µm in diameter. Structural parameters as well as an estimate of the relative content of chitin and protein in the pad material were obtained from analyzing both, Small- (SAXS) and Wide-Angle X-ray Scattering (WAXS) regions (Figure 5).

The signal in the WAXS region (Figure 5A), nominally referred to the scattering region above $q = 4$ nm^{-1}, is dominated by diffraction signal from the crystalline chitin-protein fibrils (Figure 5A). Although crystallite orientation strongly affects WAXS intensity (see SI Figure 3), integration over the scattering intensity of Bragg reflections with close to orthogonal orientation, (110) and (013) were used in order to gain qualitative information on the relative distribution of chitin in the pad (yellow scale in Figure 5B). Scattering signal from chitin crystals is observed throughout the entire pad cross-section, however with significantly lower intensity at the distal end of the pad. In this region the intensity of both (110) and (013) reflections are low, indicating that chitin density is low. In other regions–with low WAXS intensity, within the "appendix" and in the ventral wall of the pad, the (013) reflection is completely missing in the WAXS signal, indicating that the crystallites here are oriented mainly out of the section plane (SI Figure 3).

In the SAXS region the inter-fibrillar packing peak can be used to determine the packing degree of chitin-protein fibrils and their spacing (Erko, Hartmann et al. 2013). The intensity of the packing peak, related to the degree of chitin-protein fibril alignment and their orientation, is mapped in Figure 5B (magenta scale). The packing peak intensity is largest in the ventral part of the pad, and in the central part of the "appendix" (violet regions in Figure 5B). The q-position of the packing peak relates to the distance d between the fibrils by $q = 2\pi/d$. d is largest (4.82 ± 0.02 nm) in the center of "appendix", and smallest (4.59 ± 0.04 nm) at the outer cuticle layers. Sample dehydration results in a slight reduction of the inter-fibrillar distance, now ranging between 4.76 ± 0.03 nm and 4.52 ± 0.04 nm, respectively. Note that these values are exemplarily for one studied specimen only. An independent measurement of another pad section in wet state revealed an inter-fibrillar distance of 4.93 ± 0.02 nm in the appendix and 4.73 ± 0.04 nm in the outer cuticle layers, respectively, revealing small variation between samples however within a similar trend.

Fibril orientation

The in-plane orientation of chitin-protein fibrils was determined from the anisotropic azimuthal distribution of the packing peak in the SAXS region (Figure 5A). The out-of-plane

angle of the fibrils on the other hand was extracted from the angular distribution of the (110) reflection of the chitin crystal in the WAXS region according to the method described in the literature (Lichtenegger, Muller et al. 1999; Paris and Muller 2003; Seidel, Gourrier et al. 2008). The three-dimensional fibril orientation mapped in Figure 5C shows strongly varying chitin-protein fibril orientation in different regions of the pad. The ventral side of the pad and the "appendix" are dominated by out-of plane chitin-protein fibril orientation (green-, yellow- and red- bars regions in Figure 5B), while the dorsal and the distal parts of the pad are dominated by an in-plane organization of chitin-protein fibrils (blue-bars regions). This latter case may also arise from a plywood organization typical for spider cuticle (Barth 1973). In order to unequivocally determine the fibril orientation and microstructural arrangement, the same measurement and analysis were performed for two additional sections (assigned as transverse1 and transverse2 in Figure 2B) cut orthogonally to the section described in Figure 5 (SI Figure 4 and SI Figure 5). For a pure plywood organization, in-plane scattering patterns are obtained regardless of the incident beam orientation within the plywood plane, whereas a parallel fibril arrangement gives an in-plane orientation signal only when viewed perpendicular to the fibril long axis. In the transverse section in-plane fibril orientation dominates the entire sample (SI Figure 4C), indicating that the blue-bars regions in Figure 5B are characterized by a pure-plywood structure, while the green-, yellow- and red-bars regions are dominated by a parallel fiber orientation in agreement with the observations from WAXS.

Figure 5B maps the distribution of diffuse scattering intensity at low q-values ($0.4\ nm^{-1} < q < 0.6\ nm^{-1}$). The signal at such low q-values arises from electron density contrast between nanometer-sized components in the sample. These may be pores, proteins, or other molecules (e.g. sclerotization agents) within the spider cuticle. There are two prominent regions exhibiting high diffuse SAXS signal intensity (cyan regions in Figure 5B). One is close to the distal end where CLSM shows high sclerotization, the other in the center of the "appendix".

The slope of the integrated scattering intensity plotted in log-log units provides more details about the geometry of the scattering objects using the Guinier analysis (Guinier and Fournet 1955). For the wet sample a slope of -1 is found for measurements at the distal part of the pad and at the center of the "appendix". For the rest of the pad in the wet state the log-log slope equals to -2. Interestingly, in the pad's dry state the scattering intensity slope in the log-log plots equals to -2 for the entire sample.

For some regions of the pad the low-q SAXS signal discussed above shows pronounced anisotropy. In most of those cases, the anisotropy follows the same orientation as

that of the chitin signal. However, in some regions it is miss-oriented with respect to chitin. The orientation of the low-*q* SAXS signal is shown in Figure 5C together with the in-plane orientation of the chitin-protein fibrils. The region with the largest mis-orientation between the chitin signal and the low-*q* SAXS signal is in the distal part of the pad, the same region in which we find a slope of -1 in hydrated samples.

Interpretation of SAXS data: A SAXS slope of -2 in a log-log plot follows the Gaussian chain model of a randomly organized scattering object (Pedersen 1997) which we attribute the scattering of the matrix proteins (Erko, Hartmann et al. 2013). If there is no interference a slope of -1 indicates cylindrical scattering objects (Pedersen 1997). Applying the Guinier analysis (Guinier and Fournet 1955) we determined an average cylinder diameter of 4.7 ± 0.1 nm. The size of these objects is similar to the size of the chitin-protein fibrils determined before using the packing peak position. We therefore assume that the scattering objects again are chitin-protein fibrils. Importantly, the analysis indicates that these chitin-protein fibrils are loosely packed and not arranged in a lattice. Note, however, that in the same pad regions, we also detect the inter-fibrillar packing peak (albeit with different orientation), suggesting that two types of chitin-protein fibril arrangement occur in the same region of the pad.

This means that the “loose” fibrils are oriented almost perpendicular to the pad’s distal surface while the tightly packed fibrils (i.e. in twisted plywood structure) follow the curvature of the pad surface. In the dorsal region and in the “appendix” the orientations of both components coincide.

Micro-channels and lamella organization at the distal and dorsal parts of the pad

Polarized light microscopy was used to further analyze the orientation of chitin-protein fibrils in different parts of the pad. The bright regions in Figure 4D arise from chitin-protein fibrils oriented within the plane of the sample (regions parallel to the polarization angle indicated by the white cross appear dark). In accordance with the results of X-ray scattering analysis, the dorsal and distal parts of the pad appear bright due to the contribution of the in-plane chitin-protein fibrils within the plywood structure. The “appendix” region and the ventral part of the pad, however, appears dark as this region is dominated by parallel chitin-protein fibrils oriented out of the sample plane, as previously obtained from the analysis of the WAXS signal. In the distal region of the pad we observe a striation pattern roughly perpendicular to the pad surface (in the same direction as the “loose” chitin signal obtained from the analysis of the SAXS signal above).

SEM and AFM images clearly show the lamellar arrangement in the pad cuticle (Figure 6). The spacing between the lamellae, which is directly related to the rotation angle of the fibrils in the plywood structure, changes gradually from the surface towards the interior of the pad. The direction of this gradient in lamella thickness changes in opposite directions distally and dorsally on the pad. Thus, on the dorsal side the spacing between two adjacent lamellae changes from ~250 nm at the surface to ~400 nm in the interior, as commonly observed in arthropod cuticle. At the distal side the thicker lamellae are found close to the surface (~680 nm), and the lamellae become thinner (~300 nm) in the interior.

In addition, the SEM micrographs of the distal part of the pad show multiple channels a few micrometers in diameter, oriented perpendicular to the distal surface (Figure 6A) which is in the same direction as the “loose” chitin-protein fibrils and the striation pattern in the polarized light microscope.

Micromechanical characterization

Scanning acoustic microscopy (SAM) quantifies the reflectivity, *R*, of focused acoustic waves from the surface of the sample with a spatial resolution of about 1 µm. The measured values for *R* depend on the sample stiffness and its mass density. SAM data obtained from embedded and polished pad sections, measured under water, show the spatial destribution of *R* along the pad (Figure 4E). The previously observed variations in sclerotization degree and chitin-protein fibril orientation are highly correlated with the respective sound reflectivity values. The bright-coloured regions (high reflectivity) in Figure 4E correspond to the dark reddish (highly sclerotized) regions in Figure 4A. In addition, the “appendix” region shows a particularly high reflectivity. Since the stiffness is higher in the chitin-protein fibril direction, this correlates with the measured out-of-plane orientation of the fibrils in this region as determined from WAXS signal analysis. A noteworthy exception to this trend is a bright region in the center of pad. The bright line in the SAM image corresponds to the green-to-red transition region in the respective CLSM image. Note that in the absence of a measure of the sample mass density we cannot extract quantitative information regarding the elastic modulus.

For the quantitative determination of the elastic moduli, albeit at lower spatial resolution, we performed Nanoindentation experiments under hydrated conditions on the same samples at four different regions. The regions examined are assigned as A-D in Figure 4E. The results (Table 2) show large differences of the reduced elastic modulus E_r between the regions studied. The highest value of 8.3 (± 1.1) GPa was found in region A, the

“appendix” region, while in region B, the dorsal part of the pad, which shows a similar sclerotization level as the “appendix”, we measured an average value of 2.8 (± 1.3) GPa. This result is consistent with SAM results and reflects the effect of fiber orientation. Note, that the elastic modulus of chitin is roughly 4 times higer along the *c*-direction (long axis) than along the *a/b* directions (Nikolov, Petrov et al. 2010).

The highly sclerotized internal region C of the pad, is characterized by E_r = 1.0 (± 0.3) GPa. And most strikingly, the distal part, region D, shows an expremely low reduced elastic modulus of E_r = 0.1 (± 0.07) GPa. Such low values are mostly known for wet and unsclerotized cuticles of insect larvae and puparia (Vincent and Wegst 2004), and are uncommon in adult cuticles.

3. Discussion on biological relevance

The cuticular pad at the distal end of the metatarsus of *Cupiennius salei* plays an important role in the mechanical transmittance and transformation of stimuli which deflect the tarsus and stimulate the metatarsal vibration receptor. The sources of the organ's adequate stimulation are manifold. Stimuli primarily include the vibrations of the plant, on which the spider sits and which are caused by the movements of predators or prey, as well as the vibrations actively used by the spiders to communicate during courtship. However, the metatarsal lyriform organ is also stimulated by low frequency tarsal deflections as they occur during the spider's own locomotion and other behavior such as prey capture and spinning behavior and as they are typical of the vibrational background noise caused by abiotic sources like wind (Friedel and Barth 1997; Barth 2002). Upon the deflection of the tarsus the proximal end of the tarsus pushes against the distal end of the metatarsus where the pad is located. High frequency stimuli beyond ca. 40 Hz are detected with high sensitivity regarding tarsal deflection amplitudes necessary to activate the sensory cells. The viscoelastic properties of the unusually thick epicuticle of the pad represent a very effective mechanical high pass filter (Young, Chyasnavichyus et al. 2014). Low frequency stimuli (lower than about 40 Hz) require much larger tarsal deflections to be detected by the vibration receptor organ. Here we describe how the structural features of the pad allow for the transmittance of high amplitude low frequency stimuli and at the same time protect the sensory organ against over-compression and damage.

In their natural habitat spiders are also exposed to the lateral deflection of their tarsi (i.e. off the main long axis of the tarsus-metatarsus) and their vibration receptors respond to these (Barth 2002). The crescent-like shape of the pad is well suited to allow such activations, as can be seen in Figure 3C. Although other shapes might also be valid (for example a round pad), they might suffer from other drawbacks such as require more material at regions which are normally not activated. The elaborated morphology of the pad and, in particular, the sub-structure of the material of which it is made are discussed in more detail in the following.

The distal end of the pad

The distal end of the pad is extremely soft showing only 100 MPa for the reduced elastic modulus as measured in Nanoindentation experiments under hydrated conditions. In agreement with this we have also found that this pad region is highly hydrated under natural conditions and the least sclerotized part of the pad. The lamella thickness in this region

decreases from the surface inwards, which is uncommon in arthropod cuticle. Lamella thickness and chitin-protein fibril orientation were recently shown to affect water sorption capability of the cuticle (Clara et al. 2014) where large lamella swell much more than thin ones. Thus, the occurrence of thick lamella at the distal end of the pad also contributes to the hydration properties of this region together with the low sclerotization (Andersen 2010). SAXS results show that in addition to the plywood structure that forms the lamellae seen in Figure 6B-C some chitin component occurs as loosely bound chitin-protein fibrils. Upon dehydration the signal from these fibrils disappears, indicating that the fibrils are suspended in water or form gel-like material. This signal is highly anisotropic with directionality that follows the direction of multiple micro-channels observed in SEM (Figure 6A) and with polarized light microscopy (Figure 4D). We therefore suggest that these channels are filled with chitin-based gel-like material, which might also account for the large swelling in this region. The micrometer-sized channels run in a direction perpendicular to the distal end surface (towards the contact region with the tarsus). Using AFM imaging McConney et al. (McConney, Schaber et al. 2009) reported droplets of epicuticular substance secreted from pores at the surface of the pad. We suggest that these are the openings of the micro-channels observed by us. The function of this secretion is unknown. On the other hand the secretion may serve to better couple tarsus and pad during stimulus transmission, similar to insect attachment pads (Dirks and Federle 2011), however, if the secretion level is high it may act in the opposite way, i.e. as a lubricant. More study is needed in order to answer this question.

The softness (100 MPa) of the pad's distal contact region with the tarsus increases the contact area with the tarsus and allows the largest deformation upon tarsal deflection while comparatively only small displacement of the pad is observed at the contact region with the slits. In this way substrate displacements in the order of up to 200 µm, in accordance with Barth and Geethabali (Barth and Geethabali 1982) are translated to small (non-destructive) slit compressions of only few micrometers (3.5 ± 0.7 µm at $9 \pm 1°$ tarsal deflection), and over-stimulation, or slit damage is avoided. Thus the pad acts as a "bumper" damping the impact of large substrate displacements.

Internal layer of sclerotized cuticle

The interior part of the cuticle in the central region of the pad is highly sclerotized as judged from CLSM, which also endows it with a relatively high elastic modulus of 1 GPa. This specific distribution of cuticle sclerotization may imply a functional, probably mechanical role. From this region the pad is no longer deformed but displaced towards the slit

region. This is most likely owed to the stiffening in this region. In agreement with the present findings Schaber et al. (Schaber, Gorb et al. 2011) found that the force needed to deflect the tarsus against the metatarsus (ca. 1.5 mN at 4°) increases exponentially with the deflection angle. This increase of force from small deflection angles to higher ones may reflect the pad deformation behavior related to its structure, where at small angles the distal part of the pad is easily deformed and at higher angles, the internal sclerotized region might resist further deformation. The dorsal part of the pad is also highly sclerotized and is made up of dominantly twisted plywood structure with rather thin lamella. It thus provides bending stiffness to support pad displacement at higher loads and restrict the displacement.

The "appendix"

The "appendix" region of the pad is characterized by a particularly high level of cuticle sclerotization as well as a high degree of parallel arrangement of chitin-protein fibrils. The parallel fibrils are oriented out of the plane of the sample sagittal sections. This also explains the measured values for the reduced elastic modulus (of about 8 GPa) in this region for sagittal sections. A similar structure of parallel fibril orientation was also found in the ventral side of the pad section. From µCT analysis we know that these two regions are connected (Figure 2 G,H) and could therefore form a stiff frame reinforcing the entire pad. This frame together with the unusually sclerotized internal cuticle is expected to resist further pad deformation instead allow small displacement of the pad towards the slits region.

Another interesting observation is that the "appendix" ridge runs parallel to the slits of the lyriform organ and extends underneath them (see for example Figures 2C,D, 3C,D and E). We suggest that the ventral extension of the appendix helps to distribute the load to lower regions of the slits, ensuring an equal distribution of the compressive load along the long axis of the organ, perpendicular to long axis of leg and along the slit walls depth.

Conclusions

The pad was described as a high-pass filter transferring only high frequencies with high efficiency (McConney, Schaber et al. 2007). Most of this filtering occurs at the epicuticle whose viscoelastic mechanical properties were recently determined using AFM at various temperature and signal frequencies (Young, Chyasnavichyus et al. 2014). Low frequency stimuli are damped by the epicuticle and would not be transferred to the slits if applied with low amplitude. However, low frequencies below about 40 Hz and even down to 5 Hz applied with high amplitude are detected by the sensory cells of the slits (Barth and Geethabali 1982;

Molina, Schaber et al. 2009). Tarsal vertical displacements will then have to be as large as some hundreds of micrometers, corresponding to the tarsal angular tilt of ~10°. We propose a mechanism for the transmittance and filtering of the full frequency range of the biologically relevant stimuli via the pad to the metatarsal lyriform organ; our results suggest that during such substrate displacements, the tarsus pushes against the pad and deforms it by some tens of micrometers at its most distal, highly hydrated region. Beyond this region, the sclerotized region and the supporting frame (appendix and ventral pad region) resist the deformation and are displaced to push against the slits. Now, however, the displacement values are considerably scaled down to only few micrometers. In addition, the "appendix" running parallel and along the slits ensures a uniform compression roughly perpendicular to the long axes of the slits for stimuli deflecting the tarsus vertically or laterally.

Taken together with previous results on high-pass filtering properties of the pad, our results emphasize the multi-functionality of the pad allowing selective low frequency stimuli to be transferred thus allowing large relevant stimulus-frequency range. Unraveling the structural arrangement in such specialized organs may provide solutions for the design of sensory materials which are capable of detecting and filtering stimuli of signal wide range.

Acknowledgements

The authors thank Stefan Siegel, Chenghao Li, Mathieu Bennet, Bernd Bayerlein and Dmitri Fix from the Max Planck Insitute of Colloids and Interfaces and Tatjana Rack from the European Synchrotron Radiation Facility for technical assistance; and Birgit Schonert for sample preparation. We are grateful to DFG and NSF for the financial support. We thank the Department of Neurobiology of the University Vienna for providing the spiders.

Tables:

Deflection angle between tarsus and metatarsus [°] Error (± 1)	Tarsus distal side (substrate) vertical displacement [µm] Error (± 5)	Pad deformation at contact region with the tarsus [µm] Error (± 0.7)	Pad displacement at contact region with the slits [µm] Error (± 0.7)
0	0	0	0
2	66	8.4	0
4	111	14.7	0.7
7	150	23.8	2.1
9	181	29.4.	3.5

Table 1: Parameters for the static loading of the pad upon µCT experiment (sample without lateral deflection component). Deflection angle values were extracted from the microscope image analysis. The substrate vertical displacement was calculated from the distance adjusted between the Tomo-press mounting tools (fixing the metatarsus on the one side and the aluminum wedge on the other side). The pad displacement and deformation values were extracted from the µCT data analysis.

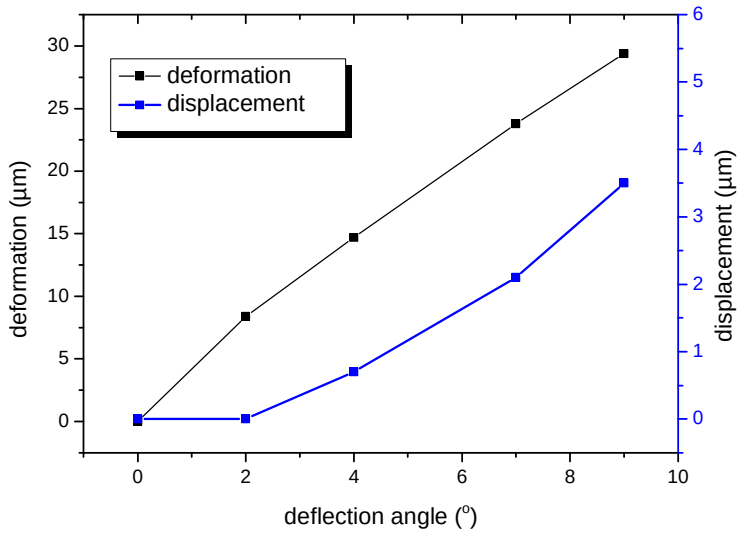

Alternative to Table 1:

@ co-authors: please tell me which you prefer better.

Measured region		Reduced Elastic Modulus [GPa]
A	appendix	8.3 ± 1.1
B	dorsal part	2.8 ± 1.3
C	sclerotized internal part	1.0 ± 0.3
D	distal part	0.1 ± 0.07

Table 2: Nanoindentation results from different parts of the sagittal section of the pad. The different regions are indicated in Figure 4E.

Andersen, S. O. (2010). "Insect cuticular sclerotization: A review." Insect Biochemistry and Molecular Biology **40**(3): 166-178.

Barth, F. G. (1969). "Fine Structure of Spider Integument .I. Walking Leg Cuticle of Adult Animals Long after Moulting." Zeitschrift Fur Zellforschung Und Mikroskopische Anatomie **97**(1): 137-&.

Barth, F. G. (1972). "Physiology of Slit Sense Organs. 1. Model Experiments on Role of Cuticular Slit in Stimulus Conduction." Journal of Comparative Physiology **78**(3): 315-336.

Barth, F. G. (1972). "Physiology of Slit Sense Organs. 2. Functional Morphology of a Mechanoreceptor." Journal of Comparative Physiology **81**(2): 159-186.

Barth, F. G. (1973). "Microfiber Reinforcement of an Arthropod Cuticle - Laminated Composite-Material in Biology." Zeitschrift für Zellforschung und Mikroskopische Anatomie **144**(3): 409-433.

Barth, F. G. (2002). A Spider's World: Senses and Behavior. Berlin, Springer-Verlag.

Barth, F. G. (2004). "Spider mechanoreceptors." Current Opinion in Neurobiology **14**(4): 415-422.

Barth, F. G. (2012). "Learning from animal sensors: The clever "design" of spider mechanoreceptors." Bioinspiration, Biomimetics, and Bioreplication 2012 **8339**.

Barth, F. G. (2012). "Spider strain detection." Frontiers in Sensing: From Biology to Engineering: 251-273.

Barth, F. G. and J. Bohnenberger (1978). "Lyriform Slit Sense Organ - Thresholds and Stimulus Amplitude Ranges in a Multi-Unit Mechanoreceptor." Journal of Comparative Physiology **125**(1): 37-43.

Barth, F. G. and Geethabali (1982). "Spider Vibration Receptors - Threshold Curves of Individual Slits in the Metatarsal Lyriform Organ." Journal of Comparative Physiology **148**(2): 175-185.

Bleuet, P., J. P. Roux, et al. (2004). "In-situ microtomography study of human bones under strain with synchrotron radiation." Developments in X-Ray Tomography Iv **5535**: 129-136.

Dirks, J. H. and W. Federle (2011). "Fluid-based adhesion in insects - principles and challenges." Soft Matter **7**(23): 11047-11053.

Douissard, P. A., A. Cecilia, et al. (2010). "A novel epitaxially grown LSO-based thin-film scintillator for micro-imaging using hard synchrotron radiation." Journal of Synchrotron Radiation **17**: 571-583.

Erko, M., M. A. Hartmann, et al. (2013). "Structural and mechanical properties of the arthropod cuticle: Comparison between the fang of the spider *Cupiennius salei* and the carapace of American lobster *Homarus americanus*." Journal of Structural Biology **183**(2): 172-179.

Fratzl, P. and F. G. Barth (2009). "Biomaterial systems for mechanosensing and actuation." Nature **462**(7272): 442-448.

Friedel, T. and F. G. Barth (1997). "Wind-sensitive interneurones in the spider CNS (Cupiennius salei): Directional information processing of sensory inputs from trichobothria on the walking legs." Journal of Comparative Physiology a-Sensory Neural and Behavioral Physiology **180**(3): 223-233.

Gingl, E., A. M. Burger, et al. (2006). "Intracellular recording from a spider vibration receptor." Journal of Comparative Physiology A **192**(5): 551-558.

Guinier, A. and G. Fournet (1955). Small-Angle Scattering of X-Rays. London, Chapman & Hall, Ltd.

Hammersley, A. P., S. O. Svensson, et al. (1994). "Calibration and Correction of Spatial Distortions in 2d Detector Systems." Nuclear Instruments & Methods in Physics Research Section a-Accelerators Spectrometers Detectors and Associated Equipment **346**(1-2): 312-321.

Hergenroder, R. and F. G. Barth (1983). "The Release of Attack and Escape Behavior by Vibratory Stimuli in a Wandering Spider (*Cupiennius Salei* Keys)." Journal of Comparative Physiology **152**(3): 347-358.

Hossl, B., H. J. Bohm, et al. (2007). "Finite element modeling of arachnid slit sensilla- I. The mechanical significance of different slit arrays." Journal of Comparative Physiology a-Neuroethology Sensory Neural and Behavioral Physiology **193**(4): 445-459.

Lichtenegger, H., M. Muller, et al. (1999). "Imaging of the helical arrangement of cellulose fibrils in wood by synchrotron X-ray microdiffraction." Journal of Applied Crystallography **32**: 1127-1133.

McConney, M. E., C. F. Schaber, et al. (2007). "Viscoelastic nanoscale properties of cuticle contribute to the high-pass properties of spider vibration receptor (Cupiennius salei Keys)." Journal of the Royal Society Interface **4**(17): 1135-1143.

McConney, M. E., C. F. Schaber, et al. (2009). "Surface force spectroscopic point load measurements and viscoelastic modelling of the micromechanical properties of air flow sensitive hairs of a spider (*Cupiennius salei*)." Journal of the Royal Society Interface **6**(37): 681-694.

Michels, J. (2007). "Confocal laser scanning microscopy: using cuticular autofluorescence for high resolution morphological imaging in small crustaceans." Journal of Microscopy-Oxford **227**(1): 1-7.

Michels, J. and S. N. Gorb (2012). "Detailed three-dimensional visualization of resilin in the exoskeleton of arthropods using confocal laser scanning microscopy." Journal of Microscopy **245**(1): 1-16.

Mirone, A., E. Brun, et al. (2014). "The PyHST2 hybrid distributed code for high speed tomographic reconstruction with iterative reconstruction and a priori knowledge capabilities." Nuclear Instruments & Methods in Physics Research Section B-Beam Interactions with Materials and Atoms **324**: 41-48.

Molina, J., C. F. Schaber, et al. (2009). "In search of differences between the two types of sensory cells innervating spider slit sensilla (*Cupiennius salei* Keys.)." Journal of Comparative Physiology A **195**(11): 1031-1041.

Nikolov, S., M. Petrov, et al. (2010). "Revealing the Design Principles of High-Performance Biological Composites Using Ab initio and Multiscale Simulations: The Example of Lobster Cuticle." Advanced Materials **22**(4): 519-+.

Oliver, W. C. and G. M. Pharr (1992). "An Improved Technique for Determining Hardness and Elastic-Modulus Using Load and Displacement Sensing Indentation Experiments." Journal of Materials Research **7**(6): 1564-1583.

Paris, O. and M. Muller (2003). "Scanning X-ray microdiffraction of complex materials: Diffraction geometry considerations." Nuclear Instruments & Methods in Physics Research Section B-Beam Interactions with Materials and Atoms **200**: 390-396.

Pedersen, J. S. (1997). "Analysis of small-angle scattering data from colloids and polymer solutions: modeling and least-squares fitting." Advances in Colloid and Interface Science **70**: 171-210.

Rasband, W. (1997-2013). "ImageJ V 1.47 " National Insitutes of Health, Bethesda MD **http://imagej.nih.gov/ij/list.html**.

Schaber, C. F., S. N. Gorb, et al. (2011). "Force transformation in spider strain sensors: white light interferometry." Journal of the Royal Society Interface **9**(71): 1254-1264.

Seidel, R., A. Gourrier, et al. (2008). "Mapping fibre orientation in complex-shaped biological systems with micrometre resolution by scanning X-ray microdiffraction." Micron **39**(2): 198-205.

Speck-Hergenroder, J. and F. G. Barth (1988). "Vibration Sensitive Hairs on the Spider Leg." Experientia **44**(1): 13-14.

Speck, J. and F. G. Barth (1982). "Vibration Sensitivity of Pretarsal Slit Sensilla in the Spider Leg." Journal of Comparative Physiology **148**(2): 187-194.

Vincent, J. F. V. and U. G. K. Wegst (2004). "Design and mechanical properties of insect cuticle." Arthropod Structure & Development **33**(3): 187-199.

Weitkamp, T., D. Haas, et al. (2011). "ANKAphase: software for single-distance phase retrieval from inline X-ray phase-contrast radiographs." Journal of Synchrotron Radiation **18**: 617-629.

Weitkamp, T., P. Tafforeau, et al. (2010). "Status and evolution of the ESRF beamline ID19." X-Ray Optics and Microanalysis, Proceedings **1221**: 33-38.

Young, S. L., M. Chyasnavichyus, et al. (2014). "A spider's biological vibration filter: micromechanical characteristics of a biomaterial surface." Acta Biomaterialia **accepted**.